Unified Simulation Methods for Quantum Acoustic Devices

Hugo Banderier[1,2,†] Maxwell Drimmer[1,2,*] and Yiwen Chu[1,2]

[1]*Department of Physics, Eidgenössische Technische Hochschule Zürich, Zürich 8093, Switzerland*
[2]*Quantum Center, Eidgenössische Technische Hochschule Zürich, Zürich 8093, Switzerland*

In circuit quantum acoustodynamics (cQAD), superconducting circuits are combined with acoustic resonators to create and control nonclassical states of mechanical motion. Simulating these systems is challenging due to the extreme difference in scale between the microwave and mechanical wavelengths. All existing techniques simulate the electromagnetic and mechanical subsystems separately. However, this approach may not be adequate for all cQAD devices. Here, we demonstrate a single simulation of a superconducting qubit coupled to an acoustic and a microwave resonator and introduce two methods for using this simulation to predict the frequencies, coupling rates, and energy-participation ratios of the electromechanical modes of the hybrid system. We also discuss how these methods can be used to investigate important dissipation channels and quantify the nontrivial effects of mode hybridization in our device. Our methodology is flexible and can be extended to other acoustic resonators and quantum degrees of freedom, providing a valuable tool for designing hybrid quantum systems.

I. INTRODUCTION

Circuit quantum acoustodynamics (cQAD) provides the opportunity to combine the unique advantages of superconducting (SC) circuits and mechanical resonators [1,2]. A device that integrates the numerous long-lived modes of compact mechanical resonators [3–5] with the strong quantum nonlinearity of SC qubits is potentially useful for quantum information processing [6–8] and tests of fundamental physics [9]. SC qubits have already been combined with a wide variety of mechanical elements, including membranes [10,11], bulk acoustic wave (BAW) resonators [12–14], surface acoustic wave resonators [15–17], and phononic crystals [18].

Finite element (FE) simulations are a crucial design tool in both circuit quantum electrodynamics (cQED) [19–24] and solid mechanics [25] for predicting the behavior of complex solid-state structures. Both fields have independently developed mature techniques that rely on different strategies and software. For example, quantum circuits are modeled using electromagnetic simulation software like Ansys HFSS [26], Microwave Office [27], or Sonnet [28], while COMSOL Multiphysics® (COMSOL) [29] is the preferred choice for performing FE simulations of acoustic resonators.

———————
*max.drimmer@phys.ethz.ch
†Present address: Oeschger Centre for Climate Change Research and Institute of Geography, Universität Bern, 3012 Bern, Switzerland.

Techniques from cQED and solid mechanics can be combined in order to simulate cQAD devices. If an electromechanical system can be modeled as a lumped element, it is possible to simulate the electromechanical response in isolation from the Josephson circuit [30,31]. This response is represented by an equivalent circuit that can be quantized to determine the system's Hamiltonian [32]. In certain cases, however, isolating an electrically small subsystem may not be possible, meaning that the system cannot be described by a simple circuit. The $\hbar$BAR [33,34], a cQAD device that features a three-dimensional (3D) transmon qubit [35] piezoelectrically coupled to a high-overtone BAW resonator (HBAR), falls into this category.

In this paper, we demonstrate two simulation approaches that unify FE techniques from cQED and solid mechanics using a single COMSOL model without the need for an equivalent circuit. In the first approach, which we call the "unhybridized eigenmode approach," we solve for the eigenmodes of the electric field and mechanical displacement field (hereafter displacement field) separately (i.e., without any piezoelectric coupling). This yields the mode structure of the unhybridized electrical and mechanical subsystems. One can then evaluate the electromechanical coupling rate between an electrical and a mechanical eigenmode using an overlap integral inside the piezoelectric material [Eq. (5)]. In the second approach, which we call the "hybridized eigenmode approach," we simultaneously solve for the coupled electric and displacement fields to find the dressed eigenmodes of the entire system. We

demonstrate this approach by first presenting a Hamiltonian formulation that extends the energy-participation ratio (EPR) method [23] to mechanical degrees of freedom. We then use it to extract important Hamiltonian parameters that arise from electromechanical coupling, such as cross-Kerr nonlinearities, anharmonicities, and mechanical EPRs in the dispersive regime. While simulating the coupled fields is more computationally intensive, the results reflect that hybridization of the electromagnetic and mechanical subsystems affects the frequency and shape of the modes, which can in turn impact the predicted coupling and loss rates.

II. HYBRID INTERACTIONS

We consider a general system consisting of an SC circuit with J transmons and $N - J$ linear electromagnetic modes interacting with a mechanical resonator supporting M modes. Even though the N linear electromagnetic modes and M mechanical modes are identically described as modes of a bosonic resonator, we use different letters to distinguish them for clarity in the rest of this section. Each of the J transmons can be described using a Hamiltonian that is a sum of a linear resonator term and a nonlinear term [32]. When the interactions are written under the rotating-wave approximation, the Hamiltonian is

$$
\frac{\hat{H}}{\hbar} = \sum_n^N \tilde{\omega}_n \hat{\tilde{a}}_n^\dagger \hat{\tilde{a}}_n + \sum_m^M \Omega_m \hat{b}_m^\dagger \hat{b}_m + \sum_{n,m}^{N,M} \tilde{g}_{nm}(\hat{\tilde{a}}_n^\dagger \hat{b}_m + \hat{b}_m^\dagger \hat{\tilde{a}}_j)
$$
$$
- \sum_{n \neq n'}^{N,N} \varsigma_{nn'}(\hat{\tilde{a}}_n^\dagger \hat{\tilde{a}}_{n'} + \hat{\tilde{a}}_{n'}^\dagger \hat{\tilde{a}}_n) - \sum_j^J \frac{E_j}{\hbar}\left(\cos\hat{\theta}_j + \tfrac{1}{2}\hat{\theta}_j^2 \right),
$$
$$(1)$$

where we have introduced $\tilde{\omega}_n$ and $\hat{\tilde{a}}_n$ (Ω_m and $\hat{b}_m$) as the frequencies and bosonic ladder operators of the nth (mth) linear electromagnetic (mechanical) resonator mode, the Josephson energy of the jth junction E_j and its flux $\hat{\theta}_j = \theta_{\mathrm{ZPF},j}(\hat{\tilde{a}}_j + \hat{\tilde{a}}_j^\dagger)$, where $\theta_{\mathrm{ZPF},j}$ are the associated zero-point fluctuations (ZPFs), and $\varsigma_{nn'}$ ($\tilde{g}_{nm}$) are the electromagnetic (electromechanical) two-mode coupling rates. The detunings between two modes are defined as $\Delta_{nn'} = \tilde{\omega}_{n'} - \tilde{\omega}_n$ and $\Delta_{nm} = \Omega_m - \tilde{\omega}_n$. The coupling between two modes is said to be *dispersive* if $|\Delta_{nn'}| \gg |\varsigma_{nn'}|$ or $|\Delta_{nm}| \gg |g_{nm}|$.

Equation (1) is a nonlinear Hamiltonian that cannot be directly modeled using standard FE simulation techniques. Instead, we follow Ref. [19] by rewriting the Hamiltonian as a sum of linear and nonlinear terms. Then we can use FE simulations to find the linear eigenmodes, from which we extract the relevant parameters that describe the nonlinear terms using the EPR method.

A. Unhybridized eigenmode approach

If we ignore the coupling between the electromagnetic and mechanical degrees of freedom [the third term in Eq. (1)], we can simulate the two subsystems individually. The results of electromagnetics-only simulations (i.e., simulations with solid mechanics and piezoelectricity turned off) are dressed eigenstates of the linear electromagnetic part of the Hamiltonian [terms 1 and 4 of Eq. (1)]. Thus, the Hamiltonian can be partially diagonalized:

$$
\frac{\hat{H}}{\hbar} = \sum_{n=1}^N \omega_n \hat{a}_n^\dagger \hat{a}_n + \sum_m^M \Omega_m \hat{b}_m^\dagger \hat{b}_m + \sum_{nm}^{N,M} g_{nm}(\hat{a}_n^\dagger \hat{b}_m + \hat{b}_m^\dagger \hat{a}_n)
$$
$$
- \sum_j^J \frac{E_j}{\hbar} \sum_{p=4}^\infty c_p \left(\sum_{n=1}^N \varphi_{nj}\hat{a}_n + \mathrm{H.c.} \right)^p.
$$
$$(2)$$

In this expression, the $\hat{a}$ are the electromagnetic ladder operators dressed by the electromagnetics-only coupling term, the c_p are the cosine expansion coefficients, and the φ_{nj} are the ZPFs of the flux in the jth junction when only dressed mode n is excited and the E_j are the jth junction's Josephson energies.

The solutions of the mechanical simulations are exactly the modes described by term 2 of Eq. (1). The electromechanical interaction is now written in terms of the dressed electromagnetic eigenmodes. The exact expression of g_{nm} depends on the nature of the interaction. Here, we consider the piezoelectric coupling that we describe in detail in Appendix A. From now on we refer to the dressed modes $\hat{a}_n, \hat{b}_m$ of this picture as "unhybridized" because the modes are either purely electrical or mechanical.

B. Hybridized eigenmode approach

As there is no conceptual difference between an electromagnetic and a mechanical mode in Eq. (1), we can equivalently choose to express the Hamiltonian in terms of $N + M$ hybrid electromechanical modes with eigenvalues ξ_k, bosonic ladder operators $\hat{c}_k$, and associated junction flux ZPFs ϕ_{kj}. That way, we obtain a Hamiltonian identical to Ref. [23] and are therefore able to apply the same method from there on. The Hamiltonian is

$$
\frac{\hat{H}}{\hbar} = \sum_{k=1}^{N+M} \xi_k \hat{c}_k^\dagger \hat{c}_k - \sum_j^J \frac{E_j}{\hbar} \sum_{p=4}^\infty c_p \left(\sum_{k=1}^{N+M} \phi_{kj}\hat{c}_k + \mathrm{H.c.} \right)^p.
$$
$$(3)$$

Under the dispersive and the perturbative assumptions detailed in Appendix B, we can limit the expansion of the

second term to $p = 4$ and keep only excitation number-preserving interactions to obtain

$$\frac{\hat{H}_{p=4}}{\hbar} = \sum_k -\Delta_k \hat{c}_k^\dagger \hat{c}_k - \frac{1}{2}\alpha_k \hat{c}_k^{\dagger 2}\hat{c}_k^2 - \sum_{l<k}\frac{1}{2}\chi_{kl}\hat{c}_k^\dagger \hat{c}_k \hat{c}_l^\dagger \hat{c}_l. \tag{4}$$

This expression highlights several experimentally relevant quantities: the $\Delta_k = \frac{1}{2}\sum_l \chi_{kl}$ are the effective Lamb shifts, the α_k are the anharmonicities, and the $\chi_{kl} = \hbar^{-1}\sum_j E_j \phi_{kj}^2 \phi_{lj}^2$ are the total cross-Kerr shifts induced between modes k and l. Under these approximations, all the parameters depend on the zero-point fluctuations of the junctions' fluxes in each mode, ϕ_{kj}. We note that in cQAD, the perturbative assumption is not always valid in the dispersive regime. However, as shown in Appendix B, the correction to these quantities can still be expressed using the same ZPFs.

In the two approaches described above, we have developed Hamiltonians with key unknowns that can be obtained from simulations. In the unhybridized eigenmode approach, they are the bare mode frequencies ω_n and Ω_m, the junction flux ZPFs in the bare electromagnetic modes φ_{nj}, as well as the piezoelectric pairwise coupling rates g_{nm}. In the hybridized eigenmode approach, we only need to solve for the hybridized mode frequencies ξ_k and the junction flux ZPFs ϕ_{kl}.

III. SIMULATING HYBRID QUANTUM DEVICES

A. Physics interfaces

We begin each simulation by choosing physics interfaces in COMSOL, each of which defines a vector field along with its equations of motion to be solved. We used the **Electromagnetic Waves, Frequency Domain** (**emw**) interface in the RF Module for modeling SC circuits and microwave cavities and used the **Solid Mechanics** (**solid**) interface in the Structural Mechanics Module for the acoustic resonator.

The second step is dynamically combining these interfaces together. In general, linking interfaces A and B is simply done by calling the field defined in A in a domain or boundary condition on B and vice versa. In many cases, COMSOL has built-in multiphysics interfaces that perform this step. However, no such interface exists between **solid** and **emw**. Therefore, the coupling must be defined manually. In this work, electromagnetic and mechanical objects are coupled by the piezoelectric effect [36]. In a piezoelectric medium, the wave equations for the electric and displacement fields are modified to become Eqs. (A23) and (A24) as derived in Appendix A. These modifications are implemented in our simulation using three additional domain conditions, represented as *nodes* of the physics interfaces. Specifically, the **effective medium** and **external current density** nodes are added to the **emw** interface

and an **external stress** node is added to the **solid** interface. A detailed description is provided in Appendix C.

B. Model of the device

We use the method presented in this work to simulate an $\hbar$BAR similar to those used in Refs. [33,34]. This device is composed of two chips: the first has one single-junction transmon qubit with one pad extended to form an antenna, and the second has a piezoelectric dome that transduces the qubit's electric field into mechanical modes of the HBAR [Fig. 1(a)]. The two substrates are bonded together such that the antenna is aligned underneath the dome [34]. Then the assembly is situated in a 3D microwave cavity [Fig. 1(b)]. cQED elements are simulated by applying a perfect electric conductor boundary condition to the superconductors (the surfaces of the microwave cavity and the leads of the qubit) and representing the Josephson junction as a lumped element inductor [19]. In our simulation, the substrate of both the qubit and HBAR chips is c-axis-oriented sapphire and the piezoelectric dome is made of c-axis-oriented aluminum nitride (AlN).

To perform a 3D full-wave eigenmode simulation of such a device, several simplifications have to be made. The whole device is symmetric about the x-z plane at $y = 0$, so we can use symmetry boundary conditions to reduce the simulation space. We observe that the long-lived modes of the HBAR are confined inside a cylindrical volume with a small transverse area in the x-y plane [Fig. 1(c)]. We therefore only simulate the mechanical fields inside a cylindrical volume with the radius of the piezoelectric dome. Finally, we simulate an HBAR with a substrate thickness of 40 μm, an order of magnitude smaller than the 420-μm-thick devices in Refs. [33,34], in order to speed up the simulations. This approximation is necessary to make the computations tractable, but it differs from experimental values where substrate thicknesses are typically about 500 μm. Using a thinner substrate does not change the operating principle of the device, so we feel that our simulations are still useful as proofs of concept, even if our numerical results are not directly comparable to any previous experiments. A detailed description of the device model can be found in Appendix C.

C. Extracting Hamiltonian parameters

An eigenmode simulation returns a set of field distributions that are labeled by their eigenfrequencies. In the unhybridized approach, these are $\underline{E}_n$ and $\underline{u}_m$. We use an overlap integral to extract the coupling rates between the unhybridized electromagnetic and mechanical modes [37],

$$g_{nm} = A_{nm}\int_{V,\text{piezo}} \underline{E}_n \cdot \underline{\underline{e}}^T : \underline{\underline{\varepsilon}}_m \, dV, \tag{5}$$
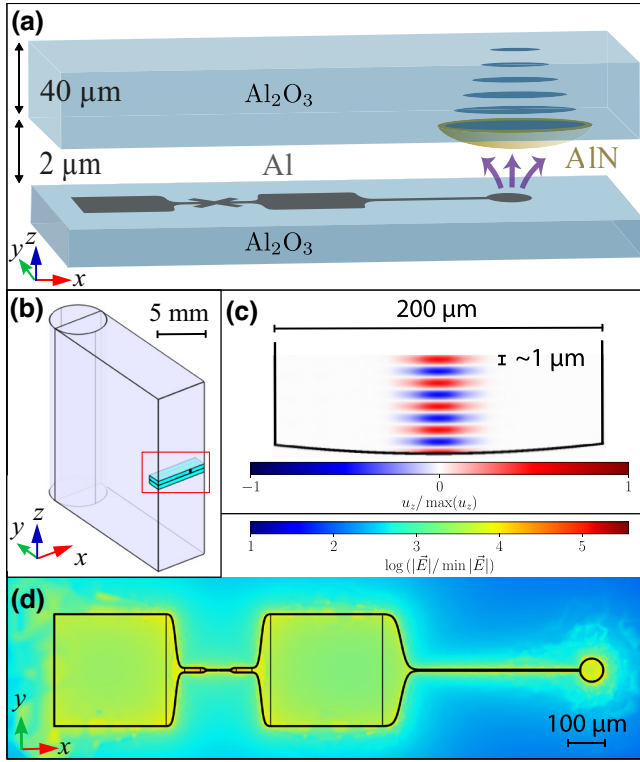
FIG. 1. Simulating the $\hbar$BAR. (a) A schematic of the $\hbar$BAR device. The bottom chip is a 3D transmon qubit, modified with an antenna (the extension at the right), on a dielectric substrate. The top chip hosts an HBAR, formed by a piezoelectric dome, positioned above the qubit antenna. The purple arrows represent the electric field of the qubitlike mode. (b) Full simulation space defined by half of a rectangular SC microwave cavity with cylindrical ends (lavender volume). The simulation is symmetric about the x-z plane closest to the viewer. The cyan structure in the red rectangle is the $\hbar$BAR. (c) Displacement field of a simulated fundamental HBAR mode in a 2D slice through the symmetry axis. This image is not to scale and is cropped to show the bottom 20% of the HBAR so that the curvature of the dome and displacement profile of the mode are clearly visible. The diameter of the HBAR and half wavelength of the acoustic mode are indicated by scale bars. (d) Electric field of the qubitlike mode centered in a region around the 3D transmon.

where $\underline{\underline{e}}^T$ is the transpose of the piezoelectric tensor, $\underline{\underline{\varepsilon}}_m$ is the strain tensor derived from $\underline{u}_m$, and the proportionality constant A_{nm} comes from normalizing the fields to that of a single photon and phonon. We justify this formula by deriving the piezoelectric Hamiltonian in a multimode Jaynes-Cummings form in Appendix A, where Eq. (A17) is the full expression for g_{nm}.

For the hybridized eigenmode simulations, we obtain the electric and displacement fields $\underline{E}_k$ and $\underline{u}_k$, respectively, for each ξ_k. COMSOL also computes several derived quantities; in this work, we make use of the electric displacement $\underline{D}_k$, strain $\underline{\underline{\varepsilon}}_k$, and stress $\underline{\underline{S}}_k$ fields, the current through the jth junction element I_{kj}, and the time-averaged global

electrical and strain energies $\overline{\mathcal{E}_{\mathrm{elec},k}}$ and $\overline{\mathcal{E}_{\mathrm{strain},k}}$. In order to use the EPR method, one must calculate the energy-participation ratio of the kth mode in the energy of the jth junction. In Appendix D, we show that the EPRs of the hybridized qubit-HBAR modes can be written as

$$p_{kj} = \frac{W_{kj}}{\overline{\mathcal{E}_{\mathrm{elec},k}} + \overline{\mathcal{E}_{\mathrm{strain},k}}}, \tag{6}$$

where the average inductive energy $W_{kj} = \frac{1}{2}L_j I_{kj}^2$ and the time-averaged electrical and mechanical energies stored in the system for mode k, $\overline{\mathcal{E}_{\mathrm{elec},k}}$ and $\overline{\mathcal{E}_{\mathrm{strain},k}}$, are defined by Eqs. (D6) and (D7) in terms of the fields $\underline{E}_k$ and $\underline{\underline{\varepsilon}}_k$. These quantities are easily obtained from the simulation solutions: L_j is the lumped element inductance that we define, while I_{kj}, the electric current through the jth lumped element, is calculated from the solution as $I_{kj} = (1/w) \int_{\mathrm{elem}\,j} \underline{J}_k \cdot \underline{t}\,dS$, where w is the junction width, $\underline{J}_k$ is the surface current, and $\underline{t}$ is a unit direction vector. In Appendix D, we show that the ZPF of the junction's flux can be written in terms of the extracted EPR

$$p_{kj} = \frac{E_j \phi_{kj}^2}{\hbar \xi_k / 2}, \tag{7}$$

which in turn defines the Hamiltonian of Eq. (3). Furthermore, the EPR can be used to calculate various loss mechanisms that arise from or are modified by the hybridization of the modes, as shown in Appendix E.

D. Finite element considerations

In finite element method (FEM) simulations, space is divided into polyhedra whose vertices define a mesh. Building this mesh, or "meshing," is done automatically in modern FE software, but some user input is almost always needed in the case of more involved geometries. Finding a mesh that is coarse enough so that the simulation runs in a reasonable amount of time but fine enough to capture all of the important physical phenomena can be challenging.

A rule of thumb for meshing FE simulations is to use at least five meshing elements per wavelength [38]. We can immediately see the issue for hybridized eigenmode simulations: the software has to simultaneously solve for $\underline{E}$ and $\underline{u}$, which have wavelengths that differ by 5 orders of magnitude at the same frequency. In the case of $\underline{u}$, for which $\lambda \sim 1\ \mu\mathrm{m}$ in typical gigahertz-frequency cQAD devices, a fine mesh can quickly make the simulation intractable if defined over too big a volume. However, we show that even in the case of an HBAR, which has a relatively large volume compared to most mechanical resonators used in cQAD systems, a meshing procedure can be found to keep the simulation at a reasonable size while resolving all of the relevant physics.

The mesh additionally needs to be optimized to reduce the number of so-called *spurious modes*. These unphysical modes are a source of inaccuracy in many FEM applications [39–41]. A handmade mesh was created in order to minimize the number of elements and spurious solutions (the meshing procedure and parameters are reported in Appendix C). Our simulations were able to solve for 150 eigenmodes in under 2 h on a computer with 64 GB of memory. Our meshing procedure drastically reduced, but could not completely eradicate, spurious modes.

IV. RESULTS

A. Unhybridized eigenmode approach

We choose to solve the unhybridized solid mechanics eigenmode simulations near a frequency corresponding to $\lambda \approx 1800$ nm in both sapphire and AlN. At this frequency, the mode has half a wavelength in the piezoelectric dome that is expected to maximize the overlap between the acoustic mode's strain field with the piezoelectrically induced external stress resulting from the qubit mode's electric field. With our geometry, this corresponds to modes with a longitudinal mode number $q = 49$. A cross section of such a mode is shown in Fig. 1(c). Because the resonator is a 3D object, it supports many modes with this longitudinal number with different patterns in the transverse plane, as well as different polarizations. We observe both Laguerre-Gaussian (LG) and Hermite-Gaussian (HG) modes in our results. The 2D profiles of these modes are represented in Fig. 2(a). Note that we always show the 2D profile corresponding to u_z irrespective of the mode's polarization; see also Appendix C 6. While we are mainly interested in longitudinal-like polarized modes [as defined in Eq. (C1)], the anisotropy of the material's piezoelectric tensor may give shearlike polarized modes nontrivial coupling to the qubit, making them interesting to study as well. We also perform an unhybridized EM simulation to compute the coupling rates, as described in the next paragraph. An example electric field distribution can be seen in Fig. 1(d), and an example displacement field distribution can be seen in Fig. 1(c) in two dimensions and Fig. 4(b) below in three dimensions.

Using these results, overlap integrals are performed between the EM qubit mode [$n = q$ in Eq. (5)] and the mechanical modes in order to compute the two-mode coupling rates g_{qm} (hereafter referred to as g for simplicity), which we plot in Fig. 2(b) against the mechanical modes' frequencies.

We find that the zeroth transverse order mode of a 40-μm HBAR has a qubit-phonon coupling rate $g \approx 2\pi \times 1$ MHz. The higher-order transverse modes have lower coupling rates due to their overlap mismatch with the qubit's electric field profile. We note that an antenna radius of $r = 20$ μm was chosen, but it could be optimized in shape
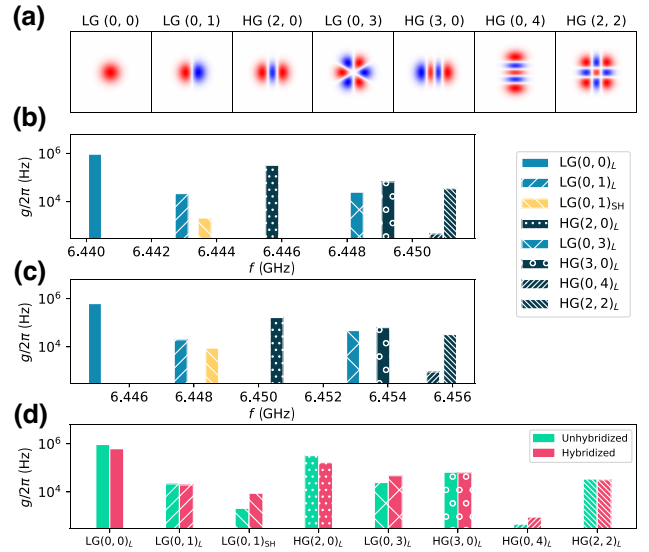
FIG. 2. Acoustic modes and electromechanical coupling rates. (a) Two-dimensional longitudinal displacement (u_z) profiles of acoustic modes observed in our simulations. (b) An acoustic spectrum with electromechanical coupling rates calculated using the unhybridized eigenmode approach. (c) An electroacoustic spectrum with electromechanical coupling rates calculated using the hybridized eigenmode approach. (d) A mode-by-mode comparison of the electromechanical coupling rates extracted from unhybridized (green) and hybridized (red) simulations. The coupling rates in (b), (c), and (d) refer to a qubit mode at $\omega = 2\pi \times 6.424$ GHz.

to increase the coupling rate to any of the observed acoustic modes.

B. Hybridized eigenmode approach

Next, we turn on the piezoelectric coupling between the **solid** and **emw** interfaces. To test our implementation and demonstrate the capabilities of this simulation framework, we perform eigenfrequency simulations while sweeping the qubit's inductance L such that the frequency of the qubitlike mode (defined as the mode with the highest EPR) intersects the set of high-overtone HBAR modes mentioned in the previous section. Note that the acoustic mode frequencies shift up by about 5 MHz compared to the uncoupled modes because the piezoelectric effect increases the stiffness of the AlN material [42].

The eigenfrequencies found in the simulations are shown in Fig. 3(a) and are plotted against the frequency of the unhybridized (UH) qubit mode. We observe avoided crossings in good agreement with the values of g computed in the previous section. This comparison between the unhybridized and hybridized approaches provides a sanity check for the physics modeling. The EPRs calculated from this frequency sweep, shown in Fig. 3(b), are another way to visualize the hybridization of the qubit with the acoustic modes. When the qubit hybridizes with a mechanical
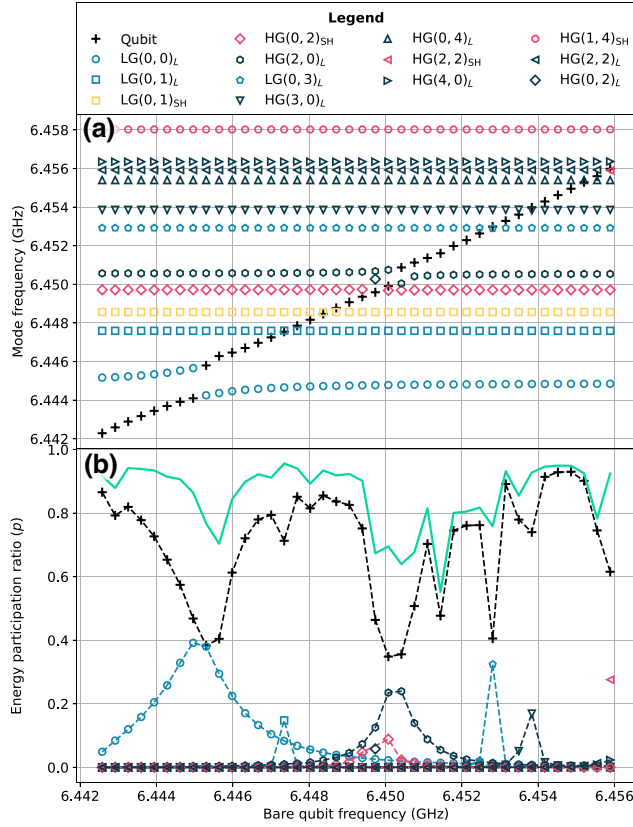
FIG. 3. Results of hybridized electromechanical simulations. (a) The mode spectrum near the acoustic fundamental longitudinal mode at $\omega = 2\pi \times 6.445$ GHz shows several avoided crossings. The size of each avoided crossing indicates the coupling between the mechanical mode and the qubit. The legend above this plot applies to both subfigures. (b) Energy-participation ratios of each mode shown in (a) to the junction. Both longitudinal-like and shearlike modes are labeled according to their u_z profiles. The green line indicates the sum of the EPRs of all of the modes in the figure.

mode, a significant fraction of the qubitlike mode EPR is allocated to the mechanical-like mode.

One challenge of analyzing these simulations is the presence of a significant number of spurious modes in the results, which are a source of inaccuracy in the derived quantities. We find them when looking for gigahertz-frequency eigenmodes of the displacement field in both unhybridized and hybridized simulations. These modes appear as several pointlike defects on mesh edges and nodes (see Appendix C 4). We observed that simulations with finer transverse meshing tended to have more spurious modes.

To address this issue, we identify the so-called "physical modes" in postprocessing by finding the modes whose displacement fields best match those of the LG and HG modes. These, together with the qubit mode, are used for further analysis, while the rest are discarded as spurious

TABLE I. Top: frequencies and EPRs of the qubitlike mode and the two most strongly coupled acoustic modes. Bottom: pairwise (cross-)Kerr couplings $\chi_{k,l}/2\pi$ between the modes.

Mode	Qubit	LG$(0,0)$	HG$(2,0)$
f (GHz)	6.424	6.445	6.451
p	0.95	1.4×10^{-3}	5.4×10^{-5}
$\chi_{k,l}/2\pi$ (Hz)	Qubit	$(0,0)$	$(1,0)$
Qubit	5.2×10^8	4.4×10^4	2.3×10^3
$(0,0)$	...	1.1×10^3	1.7×10^2
$(1,0)$	...	...	1.7×10^0

modes (see Appendix C). This process is not ideal, however, since the physical modes can be hybridized with the spurious modes through their coupling to the qubit. This causes an issue that we refer to as EPR dilution, where part of the physical mode's EPR is distributed to spurious modes with nearby frequencies. The effect of EPR dilution is evident for certain bare qubit frequencies in Fig. 3(b) where the EPRs of all the modes sum to less than one (e.g., around 6.451 GHz). Evidently, however, the effect of EPR dilution is on the 20% level.

We now focus on the case of a large detuning between the qubit mode and the same family of LG acoustic modes as in Figs. 2(b), 3(a), and 3(b) in order to demonstrate the extraction of design quantities in the dispersive regime. We choose a value for the junction inductance such that the unhybridized qubit ($k = q$) is $\Delta_{q,(0,0)}^{\mathrm{UH}} \approx 2\pi \times 21$ MHz below the LG$(0,0)$ mode. We compute the self- and cross-Kerr coupling rates using the EPRs, from which we can further compute the mode's anharmonicity $\alpha_k = \frac{1}{2}\chi_{k,k}$ and its Lamb shift $\Delta_k = \frac{1}{2}\sum_l \chi_{k,l}$.

The qubit's anharmonicity can be compared with its capacitive energy $E_C = e^2/hC$, since $\alpha_q \approx E_C/2h$ [43] for transmons. We can infer the capacitance C of the qubit from the slope of its inverse squared frequency using $\omega_q^{-2} = LC$ and obtain $C = 67$ fF, finally giving an expected anharmonicity of $E_C/2h = 288$ MHz. This is in reasonably good agreement with the EPR result of $\alpha_q = 261$ MHz (see Table I), considering that E_C/h overestimates α_q [44].

We further verify the results in Table I by using them to compute the coupling rate g between the qubit (q) and the other modes (l) with the approximate relationship [44]

$$g_{q,l}^2 \approx \Delta_{q,l}^{\mathrm{UH}} \chi_{q,l} \frac{\Delta_{q,l}^{\mathrm{UH}} + \alpha_q}{2\alpha_q}. \tag{8}$$

The mode numbers q, l refer to either unhybridized modes (on g and Δ^{UH}) or their hybridized counterparts (on χ and α). The results are shown in Fig. 2(c). Figure 2(d) shows good agreement between the g computed using the two methods we described. The discrepancies may be in part explained by EPR dilution and the approximate nature of Eq. (8).

V. OUTLOOK

We have demonstrated a technique for the simulation of cQAD devices that unifies electromagnetic and mechanical degrees of freedom under the EPR method. Importantly, we showed that quantum circuits, including SC qubits, can be combined with solid mechanics within the powerful multiphysics framework of COMSOL. By combining the necessary physics interfaces, we can extract the hybridized eigenmodes of the entire system. We showcased this technique by simulating an $\hbar$BAR, and showed that it gives results in good agreement with other methods for estimating device parameters in the dispersive regime.

Access to the hybridized eigenmodes is an interesting feature of our method. Aside from giving a clearer conceptual image of the device, it makes our approach naturally extendable to devices with more than one interaction channel, as opposed to previous techniques with unhybridized simulations. We argue that they would fail at predicting the correct results in this case because, by modifying the eigenmodes' shape, each interaction channel influences all the other's coupling strength. Similarly, our method can be used to compute quality factor contributions for dissipation channels created or heavily modified by the hybridization. We discuss this second point in Appendix E and will explore this further in the future.

The example shown in this work may be the most computationally intensive of the existing cQAD systems due to the large size of the acoustic resonator. Therefore, applying our methodology to other types of devices should prove relatively straightforward. More generally, our technique may be extended to other types of hybrid quantum systems such as SC qubits coupled to magnonic resonators [2,45] or devices where acoustic resonators interact with other qubits such as color centers [46] or quantum dots [47].

The simulation files used in this paper will be made available in the Supplemental Material [48].

ACKNOWLEDGMENTS

APPENDIX A: PIEZOELECTRIC HAMILTONIAN

In this appendix, we derive the quantum Hamiltonian for a piezoelectric solid from first principles.

1. Field quantization

We begin by quantizing the electric and displacement fields. Following the procedure in Ref. [49], we explicitly quantize the displacement field. Following Chapters 3 and 4 of Ref. [50], we define the displacement field $\underline{u}(x,t)$, strain tensor $\underline{\underline{\varepsilon}}(x,t) = \frac{1}{2}(\nabla \underline{u}(x,t) + (\nabla \underline{u})^T(x,t))$, and stress tensor $\underline{\underline{S}}(x,t)$. In an anisotropic linear material with stiffness tensor $\underline{\underline{c}}$ and density ρ, Newton's second law implies the wave equation (neglecting body forces)

$$\nabla \cdot \underline{\underline{S}} = \rho \frac{\partial^2 \underline{u}}{\partial t^2},$$
$$c_{ijlm} \frac{\partial^2 u_l}{\partial x_j \, \partial x_m} = \rho \frac{\partial^2 u_i}{\partial t^2}, \tag{A1}$$

where step 2 is written in index notation using Einstein's convention, and Hooke's law is used since we assumed a linear elastic material. We split time and space dependencies of a displacement mode assuming a frequency Ω, keeping the convention for naming frequencies from the main text (ω for electromagnetics and Ω for solid mechanics):

$$\underline{u}(x,t) = u_0 e^{-i\Omega t} \underline{h}(x) + \text{c.c.} \tag{A2}$$

Here u_0 is a constant and $\underline{h}(x)$ is a normalized function that contains the mode shape and polarization of the mode. With $u_0(t) = u_0 e^{-i\Omega t}$, we write the Hamiltonian of the system as

$$
\begin{aligned}
H &= T + V \\
&= \int dV \frac{1}{2} \rho \frac{\partial u_i}{\partial t} \frac{\partial u_i^*}{\partial t} + \int dV \frac{1}{2} c_{ijlm} \frac{\partial u_i}{\partial x_j} \frac{\partial u_l}{\partial x_m} \\
&= \frac{1}{2} \rho \Omega^2 |iu_0(t) - iu_0^*(t)|^2 \int dV |\underline{h}(x)|^2 \\
&\quad + \frac{1}{2} \int dS n_j \, c_{ijlm} u_i \frac{\partial u_l}{\partial x_m} - \frac{1}{2} \int dV u_i c_{ijlm} \frac{\partial^2 u_l}{\partial x_j \, \partial x_m} \\
&= \frac{1}{2} \rho \Omega^2 |iu_0(t) - iu_0^*(t)|^2 + 0 - \frac{1}{2} \int dV u_i \rho \frac{\partial^2 u_i}{\partial t^2} \\
&= \frac{1}{2} \rho \Omega^2 (|iu_0(t) - iu_0^*(t)|^2 + |u_0(t) + u_0^*(t)|^2) \\
&= 2\rho \Omega^2 |u_0(t)|^2, \tag{A3}
\end{aligned}
$$

where the fourth step assumes that no energy leaves the system's volume and uses the wave equation (A1) and the spatial normalization of $\underline{h}$. Here n_j is the jth element of a unit normal vector to the surface in the second term of step 3.

We define the conjugate variables

$$p = -i\Omega\rho(u_0(t) + \text{c.c}), \qquad q = (u_0(t) + \text{c.c}), \quad \text{(A4)}$$

which gives the familiar Hamiltonian

$$H = \frac{p^2}{2\rho} + \frac{1}{2}\rho\Omega^2 q^2 \tag{A5}$$

that we quantize using mechanical ladder operators

$$\hat{p} = -i\sqrt{\frac{\rho\hbar\Omega}{2}}(\hat{b} - \hat{b}^\dagger), \qquad \hat{q} = \sqrt{\frac{\hbar}{2\rho\Omega}}(\hat{b} + \hat{b}^\dagger). \tag{A6}$$

Identifying $\hat{u}_0(t) = \sqrt{\hbar/2\rho\Omega}\,\hat{b}$ lets us express the quantum displacement field as

$$\hat{\underline{u}}(\underline{x}, t) = \sqrt{\frac{\hbar}{2\rho\Omega}}\underline{h}(\underline{x})\hat{b}(t) + \text{H.c.} \tag{A7}$$

and the single mode quantum strain tensor as

$$\hat{\underline{\underline{\varepsilon}}}(\underline{x}, t) = \sqrt{\frac{\hbar}{2\rho\Omega}}\nabla\underline{h}(\underline{x})\hat{b}(t) + \text{H.c.} \tag{A8}$$

The multimode extension of this derivation is straightforward and also follows the procedure of Ref. [49]:

$$\begin{aligned}
\hat{\underline{u}}(\underline{x}, t) &= \sum_{m=1}^{M}\sqrt{\frac{\hbar}{2\rho\Omega_m}}\underline{h}_m(\underline{x})\hat{b}_m(t) + \text{H.c.} \\
&= \sum_{m=1}^{M}(\underline{u}_m(\underline{x})\hat{b}_m(t) + \text{H.c.}),
\end{aligned}$$

$$\begin{aligned}
\hat{\underline{\underline{\varepsilon}}}(\underline{x}, t) &= \sum_{m=1}^{M}\sqrt{\frac{\hbar}{2\rho\Omega_m}}\nabla\underline{h}_m(\underline{x})\hat{b}_m(t) + \text{H.c.} \\
&= \sum_{m=1}^{M}(\underline{\underline{\varepsilon}}_m\hat{b}_m(t) + \text{H.c.}).
\end{aligned}$$

Here mode m has frequency ω_m, normalized shape $\underline{h}_m(\underline{x})$, and is created (respectively annihilated) by operator $\hat{b}_m(t)$ [respectively $\hat{b}_m^\dagger(t)$].

The same derivation for the electric field gives

$$\begin{aligned}
\hat{\underline{E}}(\underline{x}, t) &= \sum_{n=1}^{N}\left(-\sqrt{\frac{\hbar\omega_n}{2\epsilon_0}}\underline{f}_n(\underline{x})\hat{a}_n(t) + \text{H.c.}\right) \\
&= \sum_{n=1}^{N}(\underline{E}_n(\underline{x})\hat{a}_n(t) + \text{H.c.})
\end{aligned}$$

with ϵ_0 the vacuum permittivity and normalized shape functions $\int_V \underline{\underline{\epsilon}}_r(\underline{x})\underline{f}_n^*(\underline{x})\underline{f}_m(\underline{x})dV = \delta_{nm}$, where $\underline{\underline{\epsilon}}_r(\underline{x})$ is the relative permittivity in the medium.

2. Piezoelectricity

Before moving on to the piezoelectric Hamiltonian, we first specify the classical piezoelectric relations we use. In a piezoelectric medium, we define the permeability $\underline{\underline{\mu}}$, permittivity at constant strain $\underline{\underline{\epsilon}}_\varepsilon$, density ρ, stiffness tensor at constant electric field $\underline{\underline{\underline{\underline{c}}}}_E$, and the piezoelectric coupling tensor $\underline{\underline{\underline{e}}}$. We write the piezoelectric constitutive relations in stress-charge from, meaning that we relate the stress $\underline{\underline{S}}$ and electric displacement $\underline{D}$ fields to the strain $\underline{\underline{\varepsilon}}$ and electric $\underline{E}$ fields:

$$\begin{pmatrix} \underline{\underline{S}} \\ \underline{D} \end{pmatrix} = \begin{pmatrix} \underline{\underline{\underline{\underline{c}}}}_E & -\underline{\underline{\underline{e}}}^T \\ \underline{\underline{\underline{e}}} & \underline{\underline{\epsilon}}_\varepsilon \end{pmatrix}\begin{pmatrix} \underline{\underline{\varepsilon}} \\ \underline{E} \end{pmatrix}. \tag{A9}$$

In this equation, the product is either a simple matrix product or a double dot product and the sum is always done on the last index(es). For example,

$$\left(\underline{\underline{\underline{\underline{c}}}}_E\underline{\underline{\varepsilon}}\right)_{ij} \equiv \left(\underline{\underline{\underline{\underline{c}}}}_E : \underline{\underline{\varepsilon}}\right)_{ij} = \sum_{k,l} c_{E,ijkl}\varepsilon_{kl}, \tag{A10}$$

$$\left(\underline{\underline{\epsilon}}_\varepsilon\underline{E}\right)_i = \sum_j \epsilon_{\varepsilon,ij}E_j. \tag{A11}$$

3. Electromechanical coupling

The stored electric and mechanical energies in a system at any time can simply be written as

$$\mathcal{E}_{\text{elec}}(t) = \frac{1}{2}\int \underline{E}(\underline{x}, t) \cdot \underline{D}^*(\underline{x}, t)dV, \tag{A12}$$

$$\mathcal{E}_{\text{strain}}(t) = \frac{1}{2}\int \underline{\underline{S}}(\underline{x}, t) : \underline{\underline{\varepsilon}}^*(\underline{x}, t)dV. \tag{A13}$$

From these and the piezoelectric constitutive relations, the added energy due to piezoelectricity is given by

$$\mathcal{E}_{\text{piezo}}(t) = -\int dV\underline{E}(\underline{x}, t) \cdot \underline{\underline{\underline{e}}}^T : \underline{\underline{\varepsilon}}(\underline{x}, t), \tag{A14}$$

which can finally be expanded in terms of the ladder operators

$$\hat{H}_{\text{piezo}} = -\hbar\sum_{nm}g_{nm}(\hat{a}_n + \hat{a}_n^\dagger)(\hat{b}_m + \hat{b}_m^\dagger), \tag{A15}$$

where we have switched to Schrödinger's picture [$\hat{a}(t) \to \hat{a}$, $\hat{b}(t) \to \hat{b}$] to remain consistent with the main text and the EPR method, and with

$$g_{nm} = \frac{1}{2}\sqrt{\frac{\omega_n}{\rho\epsilon_0\Omega_m}}\int dV(f_n^i)^*(\underline{x})e_{ijk}(\nabla\underline{h}_m)^{jk}(\underline{x}). \tag{A16}$$

In quantities that can be easily extracted from simulation results, the coupling rate between the nth electromagnetic

and the mth mechanical mode can be expressed as

$$\frac{g_{nm}}{2\pi} = \frac{\sqrt{(\omega_n/\Omega_m)(1/\rho\epsilon_0)} \int_{V,\text{piezo}} \underline{E}_n^*(\underline{x}) \cdot \underline{\underline{e}}^T : \underline{\underline{\varepsilon}}_m(\underline{x}) dV}{4\pi \sqrt{\int_V \underline{E}_n^{*T}(\underline{x}) \underline{\underline{\epsilon}}_r \underline{E}_n(\underline{x}) dV} \sqrt{\int_{V,\text{SM}} \underline{u}_m^*(\underline{x}) \cdot \underline{u}_m(\underline{x}) dV}}.$$

(A17)

We compute Eq. (A17) for all solutions of the pure SM simulation using COMSOL's feature **Volume Integration** in the piezoelectric medium, calling the E field from a chosen solution of the pure EM simulation using COMSOL's operator `withsol`. For example, one term contributing to the integrand in the numerator of Eq. (A17) therefore looks like

```
conj(withsol("sol2", sext11))
   * solid.eXX,                  (A18)
```

where `sol2` refers to the solution of the pure EM simulation, `sext11` refers to the 11 components of the external stress $\underline{\underline{S}}_{\text{ext}} = -\underline{\underline{e}}^T \cdot \underline{E}$, and `solid.eXX` refers to the 11 components of the strain tensor.

4. Electromagnetic-elastomechanical wave equation in a piezoelectric medium

We can now derive the full wave equation by using the piezoelectric relations (A9) along with Maxwell equations, where $\underline{J}$, $\underline{H}$, and $\underline{B} = \underline{\underline{\mu}}\underline{H}$ are the electric current, magnetic, and magnetic flux fields, respectively, and ρ_e is the electric charge density:

$$\nabla \times \underline{E} = -i\omega\underline{B},$$ (A19)

$$\nabla \times \underline{H} = \underline{J} + i\omega\underline{D},$$ (A20)

$$\nabla \cdot \underline{B} = 0,$$ (A21)

$$\nabla \cdot \underline{D} = \rho_e.$$ (A22)

We combine the two first Maxwell equations together with (A9) to write a first equation of motion for the electric field

$$\nabla \times \underline{\underline{\mu}}^{-1}\nabla \times \underline{E} - \omega^2\underline{\underline{\epsilon}}_\varepsilon\underline{E} = \omega^2\underline{\underline{e}} : \underline{\underline{\varepsilon}}.$$ (A23)

While combining Eq. (A1) with Eq. (A9) gives

$$\nabla \cdot \left(\underline{\underline{c_E}} : \underline{\underline{\varepsilon}}\right) + \rho\omega^2\underline{u} = \nabla \cdot \left(\underline{\underline{e}}^T \cdot \underline{E}\right).$$ (A24)

APPENDIX B: cQAD DISPERSIVE REGIME CONSIDERATIONS

The form of the Hamiltonian in Eq. (4) requires the dispersive regime assumption for all interacting pairs of two electromagnetic modes (n, n'), $|\Delta_{nn'}| \gg |\varsigma_{nn'}|$, and for all

pairs of an electromagnetic and a mechanical mode (n, m), $|\Delta_{nm}| \gg |g_{nm}|$. It also requires the perturbative assumption

$$\Delta_{kl}^H \gg \frac{E_j}{\hbar}\langle\hat{\phi}_j\rangle^p \quad \text{for all } k, l, j \text{ and all } p \geq 4$$

expressed in the hybridized eigenmode approach ("H"), with $\Delta_{kl}^H := \xi_l - \xi_k$.

This condition is usually satisfied in cQED, but not always in cQAD [34,51,52]. For example, in the case analyzed in the main text, with a single junction labeled $j = 0$, the second assumption is not respected, as $\Delta_{q,(0,0)}^H = 21$ MHz $< E_0\phi_{q0}^4/\hbar = 310$ MHz, where q refers to the qubit mode. This intermediate regime requires an additional transformation to go from the fourth-order expansion of Eq. (3) to Eq. (4), namely, a Schrieffer-Wolff transformation that removes the term proportional to $\sum_{l\neq q} \hat{c}_q^\dagger\hat{c}_q\hat{c}_l^\dagger\hat{c}_q + \text{H.c.}$, which has a time dependence of frequency Δ_{ql}^H and therefore cannot be neglected in the rotating-wave approximation. Using Ref. [43], in the simple case of a single acousticlike mode l with $\phi_{l0} \ll \phi_{q0}$, this changes the expression for the cross-Kerr coupling rates from $E_0\phi_{q0}^2\phi_{l0}^2/\hbar$ to $(E_0/\hbar)\phi_{q0}^2\phi_{l0}^2/(1 + \alpha_q/\Delta_{ql}^H)$. We can see that this correction has a significant effect for large α_q/Δ_{ql}^H ratios, which is the case in our results. In terms of the EPRs, the qubit's anharmonicity does not change, but the cross-Kerr couplings become

$$\chi_{ql} = \frac{\hbar}{E_0}\frac{\xi_q\xi_l p_q p_l}{4}\left(1 + \frac{\hbar}{E_0}\frac{\xi_q^2 p_q^2}{8\Delta_{ql}^H}\right)^{-1}.$$ (B1)

APPENDIX C: COMSOL SIMULATION SETUP

In COMSOL, all the information needed for a simulation is stored in a single file that, in the software, presents itself as a tree with several levels of nodes. At the top level there is the file node, which consists of global definitions, components, studies, and results. In a component node, we can define a model's geometry, meshing options and most importantly the physics interfaces, defining which fields will be solved in the model along with their equations of motion. Each of these nodes also feature subnodes that give additional details. In physics interfaces, the subnodes can be domain conditions, such as the main equation of motion or initial values, or boundary conditions like **fixed** or **free**.

1. Geometry in detail

The geometry consists of a $5 \times 30.5 \times 17.8$ mm^3 3D microwave cavity with two sapphire substrates: a bottom one (the qubit substrate, $5 \times 2.6 \times 0.420$ mm^3) on top of which the transmon and its antenna sit and a top one (the HBAR substrate, $5 \times 2.6 \times 0.04$ mm^3) that features the piezoelectric dome, made of AlN, looking down above

the antenna. The two substrates are 3.0 μm apart in the z direction and the piezoelectric dome has a 100-μm radius and a 900-nm maximum height. These are typical values for the devices used in Refs. [13,33,34], with the exception of the substrate thickness, which is reduced from the experimental value of 420 to 40 μm in order to reduce the mechanically active area and make the simulations computationally tractable.

As a further simplification, since the whole geometry is symmetric about the x-z plane at $y = 0$, the model is cut in half there (axis definitions can be seen in Fig. 1) and symmetry boundary conditions are used.

Since we observed that the elastic waves excited in the HBAR by this configuration were well confined to a small region in the x-y plane, we define a cylinder cut of the HBAR substrate of the same radius as the piezoelectric dome. We only solve for the displacement field inside of this cylinder instead of the whole HBAR substrate to avoid extending the required fine mesh any more than necessary. The boundaries of this cylinder cut are modeled as low reflecting boundaries to avoid any unphysical reflections.

2. Physics modeling

A 3D microwave cavity is simply empty space surrounded by a perfect electric conductor (PEC). In most FE software, modeling the PEC is done using a boundary condition of the same name, which avoids having to model an actual layer of metal that would need to be meshed and would make the simulation more complex. Losses can be modeled using either scattering boundary conditions or perfectly matched layers on certain parts of the exterior boundary that correspond to physical objects such as input and output ports.

The transmon qubit is drawn as a 2D object. The superconducting aluminum can simply be modeled as a PEC, while the Josephson junction is modeled as a linear inductance using a lumped element boundary condition. This recipe without the lumped element can be used to model coplanar waveguides or 2D resonators. All the nodes used in the **Electromagnetic Waves** physics interface are detailed here.

1. *Domain conditions.*

(a) The **Wave Equation, Electric** node is applied to all domains. It defines the equations of motion for the electromagnetic part of the simulation—the Helmholtz equation in the frequency domain. Without any additional node, this equation reads

$$\nabla \times \underline{\underline{\mu}}^{-1} \nabla \times \underline{E} - \omega^2 \underline{\underline{\epsilon}} \underline{E} = 0.$$

(b) The **effective medium 1** subnode defines a modified relative susceptibility

$$\underline{\underline{\tilde{\epsilon}}}_r = \underline{\underline{\epsilon}}_{r,\text{AlN}} - \frac{1}{\epsilon_0} \underline{\underline{e}} : \left(\underline{\underline{\underline{e}}} : \underline{\underline{\underline{c_E}}} \right)^T,$$

and applies it to the domain corresponding to the piezoelectric dome. This is the first of three steps for piezoelectric implementation.

(c) The **External Current Density** node adds a source term of the form $-i\omega \underline{J}_{\text{ext}}$ to the right-hand side of the Helmholtz equation for the domain corresponding to the piezoelectric dome. We define $\underline{J}_{\text{ext}} = i\omega \underline{\underline{e}} : \underline{\underline{\epsilon}}$. This is the second step for piezoelectric implementation.

2. *Boundary conditions.*

(i) The **Perfect Electric Conductor 1 & 2** nodes define perfectly reflecting boundaries for the electromagnetic fields. The first node is applied to the exterior boundaries (sides of the cavity) while the second one is applied to the transmon's geometry parts since it is implemented as a 2D object. The boundary equation is simply $\underline{n} \times \underline{E} = 0$, where $\underline{n}$ is a normal vector to the boundary element.

(ii) The **Lumped Element** node acts like a linear circuit containing at most a resistor, a capacitor, and an inductor. It has to be connected to conductors (perfect electric conductors in our case) on two sides. We use it to act like the linear part of our Josephson junction, so we define it as an inductor.

(iii) The **Perfect Magnetic Conductor** node is simply a symmetry boundary condition for the electric field. This allows us to cut the whole system in half along the x-z plane at $y = 0$ since the system is the same on both sides.

For the **Solid Mechanics** interface, which is only solved for in the piezoelectric dome and a cylinder cut of the HBAR above it, with the same height as the top substrate and the same radius as the dome, we have the following conditions.

1. *Domain conditions.*

(a) The **Linear Elastic Material** node defines the equations of motion for the solid mechanics part of the simulation in all selected domains (piezoelectric dome and HBAR cylinder cut). The equation is the standard elastic wave equation: $\nabla \cdot \underline{\underline{S}} + \rho \omega^2 \underline{u} = 0$. Without additional nodes we have $\underline{\underline{S}} = \underline{\underline{c_E}} : \underline{\underline{\epsilon}}$.

(b) The **External Stress** subnode adds the external stress $\underline{\underline{S}}_{\text{ext}} = -\underline{\underline{e}}^T \cdot \underline{E}$ to $\underline{\underline{S}}$ in the domain corresponding to the piezoelectric slab. This is the third and final step for piezoelectric implementation.

(c) The **Prescribed Displacement** node can be used to simplify the simulation to only include the z component of the displacement field u_z, leaving u_x and u_y at 0 everywhere. This has been shown to be a very good approximation, while drastically reducing the number of spurious modes in the results of the simulation.

2. *Boundary conditions.*

(i) The **Free** boundary condition is applied on the sides and bottom of the piezoelectric dome and on top of the HBAR.

(ii) The **Low-Reflecting Boundary** node is used to avoid reflection on the unphysical boundaries on the side of the HBAR's cylinder cut. Note that a perfectly matched layer is usually preferred to this kind of boundary condition, but unfortunately in our case it cannot be implemented.

(iii) The **Symmetry Boundary Condition** node is used on the boundaries of the x-z plane at $y = 0$ to cut the system in half as well.

3. Meshing procedure

To properly mesh the HBAR, we need to respect the rule of thumb of five elements per wavelength in the longitudinal direction while also resolving higher-transverse-order modes since we expect non-negligible coupling to them. In addition to increasing the simulation size, a finer transverse mesh was also observed to increase the number of spurious modes (see the next section). Because no simple metric characterizing the spurious modes is directly available in COMSOL's results, an automatic mesh refinement study could not be used to limit their presence.

For our model, a handmade mesh was created for the part of the geometry where solid mechanics are solved using a **mapped** and a **swept** node, which allow us to control the number of meshing points in all three cylindrical directions using **distribution** subnodes. For all simulations whose results are reported in this work, the cylindrical region is divided into a shell with inner radius 30 μm and a **mapped** mesh with ten azimuthal and six radial elements and center region, which is a free quad surface mesh with maximum element size 5 μm. The rest of the simulation space can then be meshed with automatically generated tetrahedrons, where the only user inputs are size specifications. We observed that the parameters with the most impact were the maximum element size and z-stretching ratio. A light convergence analysis was performed to ensure that the meshing was sufficiently dense near the junction where a strong electric field gradient can be found. Using this meshing procedure, a hybridized eigenmode simulation finds 150 modes in 2 h on a computer with 64 GB of memory.

4. Spurious modes

FE eigenmode simulations can converge to modes that are not physical, referred to as spurious modes [39–41]. In our simulations, only the solid mechanics part has this problem. These spurious modes give field distributions made out of point defects situated on mesh points similar to that shown in Fig. 4. After extensive testing, we can only speculate that the spurious modes we observe are the results of numerical instabilities coming from a combination of the high frequency of the simulations, the small mesh features, and the full-3D nature of the problem being solved, as only when these three features coexist did we
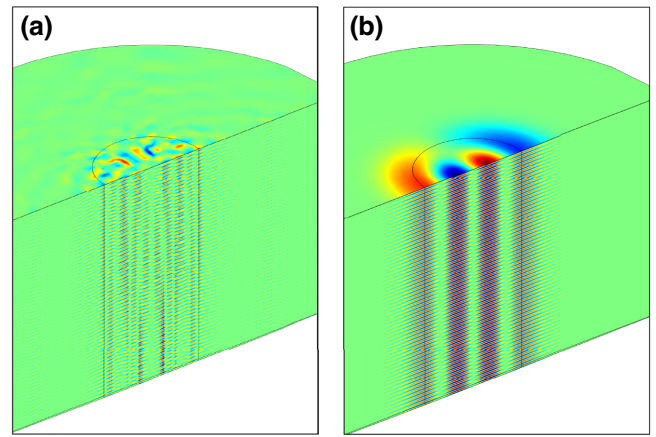
FIG. 4.   Illustration of two modes with neighboring frequencies in an unhybridized solid mechanics simulation: (a) a spurious mode and (b) a physical LG(1, 1) mode.

observe this problem. These modes can appear in greater numbers than physical modes, which causes two problems. First, if one wants to find a certain number of modes (higher-order transverse modes of the HBAR in our case), one typically has to ask the solver for many more modes than this number. Thus, the presence of spurious modes in the results artificially increases the solve time.

Another detrimental effect of the spurious modes is "EPR dilution," where the EPR of a physical mode will be shared among several spurious modes that are nearby in frequency. The coupling of the qubit mode to a spurious mode is typically of the order of 1 kHz, but in certain cases the frequency difference between a spurious mode and a physical or qubit mode can be lower, creating a significant
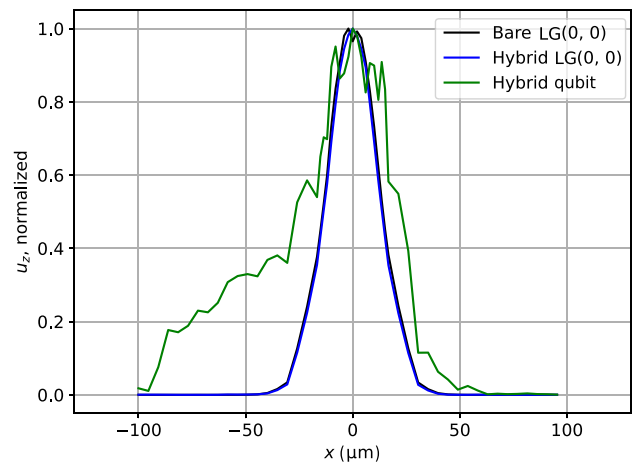
FIG. 5.   Acoustic displacement along a line defined by the interface between the piezoelectric dome and the sapphire and the symmetry axis of the simulation ($y = 0$). The sharp features on the qubit mode are the result of hybridization with spurious modes.

hybridization in the hybrid simulations. This reduces the value of the physical or qubit mode's EPR and the quantities obtained through it, such as the cross-Kerr coupling rate.

No method was found to entirely remove spurious modes from the results of solid mechanics eigenmode simulations of an HBAR. The solutions proposed in Refs. [39–41] did not give satisfactory results, which led us to believe that the root of the problem is also different. We observed that the spurious modes were largely independent of the mesh settings, but disappear once the simulation frequency is reduced to a few hundred megahertz. We also could not find any one-number metric that distinguishes them from physical modes, and their estimated convergence error (using COMSOL's error estimates for example) is lower than that of the physical modes, meaning that stronger convergence requirements make this issue worse. The only two things one can do to mitigate this problem is optimize the meshing (previous section) and postprocess the data.

5. Solver settings and convergence

All simulations used in this work are done using "eigenmode" COMSOL studies that uses a direct MUMPS solver, with most settings kept as default. However, in the case of hybridized simulations, one change needs to be done in order for the solver to converge to sensible results [53]. The COMSOL settings "Scaling" and "Residual Scaling" should be set to 10^2 for the electric field $\vec{E}$ and to 10^{-20} for the displacement field $\vec{u}$. This is done in the nodes found under **Study ▶ Solver Configurations ▶ Solution ▶ Dependant variables**.

6. Acoustic polarization and postprocessing

After the results are computed by COMSOL, we apply a postprocessing procedure in order to extract quantities of interest from the simulation. We expect the physical eigenmodes of the HBAR to include Laguerre-Gaussian or Hermite-Gaussian modes with longitudinal (component 33 of $\underline{\varepsilon}$) or shear (components 13 or 23) polarization. These modes admit an analytical expression for their longitudinal mode profile (u_z at the top surface). By computing the pointwise distance between the mode profiles of each eigenmode in the results and these analytical mode profiles, we can find the best match in the results, and simply assign all results that are not good fits for any of the reference modes as spurious modes. Additionally, the longitudinal or shear nature of a physical eigenmode can be simply extracted using, for example, the weight of a tensor component in the strain energy of the mode. Formally, the polarization is attributed to component c, with c in {11, 12,

13, 21, 22, 23, 31, 32, 33}, if c respects

$$\frac{(1/4)\text{Re} \int_{V,\text{SM}} S_c(\underline{x}) : \varepsilon_c^*(\underline{x}) dV.}{\overline{\mathcal{E}_{\text{strain},k}}}$$
$$> \frac{(1/4)\text{Re} \int_{V,\text{SM}} S_{\tilde{c}}(\underline{x}) : \varepsilon_{\tilde{c}}^*(\underline{x}) dV.}{\overline{\mathcal{E}_{\text{strain},k}}} \quad \text{(C1)}$$

for all other components $\tilde{c}$. To keep things simple, all physical modes are recognized and labeled according to their u_z profiles. For other mechanical resonator geometries, physical modes can usually also be visually distinguished from spurious ones, but a similar automated method for distinguishing them from spurious modes may need to be developed.

APPENDIX D: HYBRID EPR METHOD

The goal of the EPR method, developed by Minev *et al.* [23], is to compute the coefficients of the cQED Hamiltonian from the so-called energy-participation ratios. We mirror a simplified version of the derivation from this paper but in the case of a hybrid Hamiltonian [Eq. (3)].

The energy of a classical mechanical resonator's eigenmode oscillates in time between strain and kinetic energies. Analogously, for a classical electronic circuit, it oscillates between inductive and capacitive energies. In the unhybridized eigenmode approach, for each mechanical (electromagnetic) oscillator in the system, the time-averaged strain (*linear* inductive) energy is equal to the time averaged kinetic (capacitive) energy. Equivalently, each form of the energy's time average is equal to half the time-averaged total linear [54] energy for this mode:

$$\overline{\mathcal{E}_{\text{lin. ind},n}} = \overline{\mathcal{E}_{\text{elec},n}} = \tfrac{1}{2}\overline{\mathcal{E}_{\text{total, EM},n}},$$
$$\overline{\mathcal{E}_{\text{strain},m}} = \overline{\mathcal{E}_{\text{kin},m}} = \tfrac{1}{2}\overline{\mathcal{E}_{\text{total, mech},m}}. \quad \text{(D1)}$$

Here $\mathcal{E}_{\text{lin. ind},n}$ is the sum of the energy stored in the magnetic field $\mathcal{E}_{\text{mag},n}$ as well as the energies of the lumped element inductances $\sum_j \tfrac{1}{2} L_j I_{nj}^2$. The EPR is then defined as [23]

$$p_{kj} := \frac{\text{linear inductive energy in junction } j \text{ in mode } k}{\text{total linear inductive energy in mode } k}. \quad \text{(D2)}$$

In the hybridized eigenmode approach, the definition of the total linear inductive energy in mode k is extended to include the strain energy:

$$\overline{\mathcal{E}_{\text{lin. ind},k}} + \overline{\mathcal{E}_{\text{strain},k}} = \overline{\mathcal{E}_{\text{elec},k}} + \overline{\mathcal{E}_{\text{strain},k}}$$
$$= \tfrac{1}{2}\overline{\langle \hat{H}_{\text{lin}} \rangle_k}$$
$$= \frac{\hbar}{2} \sum_{l=1}^{N+M} \xi_l \langle \hat{c}_l^\dagger \hat{c}_l \rangle_k. \quad \text{(D3)}$$

We have introduced $\overline{\bullet}$ as the time average and $\langle\bullet\rangle_k$ as the expectation value of an operator over a state with excitations in a single mode. The numerator of Eq. (D2) is unchanged since a junction's inductive energy does not include any mechanical part. It is defined as the time-averaged linear inductive *excitation* energy (as opposed to the absolute energy) at junction j when only mode k is excited:

$$\overline{\left\langle \tfrac{1}{2}E_j \hat{\phi}_j^2 \right\rangle_k} - \overline{\left\langle \tfrac{1}{2}E_j \hat{\phi}_j^2 \right\rangle_0}. \tag{D4}$$

Defining a general Fock state for this system as

$$|\mu_1, \ldots, \mu_{N+M}\rangle,$$

we see that writing the EPR in terms of a single-mode Fock state makes it independent of the excitation number and links it to the ZPF of the junction's flux:

$$p_{kj} = \frac{\langle\mu_k|(E_j\hat{\phi}_j^2/2)|\mu_k\rangle - \langle 0|(E_j\hat{\phi}_j^2/2)|0\rangle}{(1/2)\sum_l^{N+M} \hbar\xi_l\langle\mu_k|\hat{c}_l^\dagger\hat{c}_l|\mu_k\rangle} = \frac{E_j\phi_{kj}^2}{\hbar\xi_k/2}. \tag{D5}$$

In practice, we extract the denominator of Eq. (D2) by performing finite-sum integrals over the volumes where the fields $\underline{E}$ and $\underline{u}$ are defined:

$$\overline{\mathcal{E}_{\mathrm{elec},k}} = \frac{1}{4}\mathrm{Re}\int_V \underline{E}_k(\underline{x})\cdot\underline{D}_k^*(\underline{x})dV, \tag{D6}$$

$$\overline{\mathcal{E}_{\mathrm{strain},k}} = \frac{1}{4}\mathrm{Re}\int_{V,\mathrm{SM}} \underline{\underline{S}}_k(\underline{x}):\underline{\underline{\varepsilon}}_k^*(\underline{x})dV. \tag{D7}$$

APPENDIX E: MODELING DISSIPATION

Our simulation framework can also be used to study dissipation in cQAD devices. In this appendix, we introduce the basics for this next step in the method. The relevant loss mechanisms in a $\hbar$BAR-like device can be separated into two different categories based on how they can be estimated using simulations. In the first case, which we call *semianalytical loss*, a lossy element (surface or volume) has an intrinsic quality factor that is taken from the literature. Then, its participation in the overall quality factor is weighted by the element's energy-participation ratio that is computed from the results of the simulation. These ratios are referred to as "lossy" EPRs to distinguish them from the junction EPRs discussed in the rest of the paper, even though the principle is the same. In this appendix, we illustrate three examples of such dissipation mechanisms: bulk dielectric and surface inductive losses [23,55,56] as well as losses due to surface roughness in the acoustic resonator. The second category of losses includes mechanisms that

can be fully characterized numerically, so we call it *numerical loss*. One such mechanism present in our system is so-called phonon diffraction loss, where we consider all phonons leaving the center region of the HBAR as lost and quantify this using a numerical flux integration.

1. Semianalytical loss calculations

For a given EPR-based loss mechanism $\mathcal{L}$, its overall contribution to a mode's quality factor is a weighted inverse sum with contributions from all lossy elements

$$\frac{1}{Q_k^{\mathcal{L}}} = \sum_l \frac{p_{kl}^{\mathcal{L}}}{Q_l^{\mathcal{L}}}. \tag{E1}$$

Bulk dielectric losses of the electromagnetic field are characterized by the loss tangent δ_l of a lossy solid l. This loss tangent is the inverse of an intrinsic quality factor Q_l^{diel}, and the contribution to the overall quality factor of a mode from one such solid is weighted by its energy-participation ratio

$$p_{kl}^{\mathrm{diel,\,bulk}} = \frac{1}{\mathcal{E}_k}\frac{1}{4}\mathrm{Re}\int_{V_l} \underline{E}_m^*\cdot\underline{\underline{\epsilon}}\,\underline{E}_m dV. \tag{E2}$$

We have defined the total energy of mode k as $\mathcal{E}_k = 2\overline{\mathcal{E}_{\mathrm{elec},k}} + 2\overline{\mathcal{E}_{\mathrm{strain},k}}$ [see Eq. (D1)].

Surface inductive losses are caused by surface currents and result in Ohmic loss. These are characterized by an intrinsic quality factor estimated at unity for metals such as the copper of the microwave cavity, and higher than 10^5 for SC aluminum [23]. The contribution of a lossy surface l is computed using

$$p_{kl}^{\mathrm{ind,\,surf}} = \frac{1}{\mathcal{E}_k}\frac{\lambda_l\mu_l}{4}\mathrm{Re}\int_{\mathrm{surf}_l} \underline{H}_{k,\parallel}^*\cdot\underline{H}_{k,\parallel}ds, \tag{E3}$$

where λ_l is the skin depth of the surface's material and μ_l its permeability.

Acoustic losses due to surface roughness are estimated using a method from Ref. [57]. Surface roughness limits the quality factor to

$$Q_k^{\mathrm{rough}} = \frac{h^2}{2n_k\sigma^2},$$

where n_k is the longitudinal mode number, $\sigma^2 = \langle z^2\rangle$ is the height variance of the surface assuming a Gaussian-distributed roughness, and h is the height of the HBAR such that $|\underline{q}_k|h = n_k\pi$, where $\underline{q}_k$ is the mode's wave vector. This quality factor only applies to the HBAR, so it has to be weighted by the fraction of energy stored in the mechanics $2\overline{\mathcal{E}_{\mathrm{strain},k}}/\mathcal{E}_k$.

2. Numerical loss calculations

The planoconvex shape of the HBAR was chosen to provide both longitudinal and transverse confinement to the acoustic modes. However, to study the effect of imperfections in this geometry, such as the finite size of the dome, we can use simulations to calculate the acoustic energy leaving the Fabry-Pérot cavity (the region of the sapphire substrate above the piezoelectric dome). This can be treated as loss because, even if the substrate has a finite size and reflecting boundaries, the timescale on which the energy is reflected back into the mode region is much longer than the typical timescale of operations we are interested in [33,34]. We compute a quality factor due to *diffraction loss* using a flux integral of the mechanical Poynting vector $\underline{P}_a$,

$$Q_k^{\mathrm{diff}} = \omega_k \frac{\mathcal{E}_k}{\int_{S_d} \underline{P}_a \cdot d\underline{\sigma}}. \tag{E4}$$

Here S_d is a cylindrical surface that defines the boundary of the acoustic cavity, and is parametrized by $(x_0 + R\cos\theta, R\sin\theta, z)$, where $x_0 = 1$ mm is the position of the center of the antenna, $R = 90$ µm, $\theta \in [-\pi/2, \pi/2]$, and $z \in [-0.9, 40]$ µm, which includes the entire height of the substrate.

3. Effects of hybridization on losses

An interesting new feature that arises from our simulation framework is the ability to study mechanical losses in hybrid qubit- or cavitylike modes, and electromagnetic losses in mechanical-like modes. These new effects can only be studied once one has access to the full dynamics of the hybridized eigenmodes and are thus a unique feature of the hybridized approach.

As an example, we show how the qubit mode, once hybridized with the HBAR in the same dispersive regime as in the main text, acquires a new loss channel through phonon diffraction. Figure 5 shows the LG(0, 0) mode of the unhybridized and hybridized simulations as well as the qubitlike mode in the hybridized simulation. The displacement profile of the bare mechanical mode (black) and the hybridized mechanical-like mode (green) are almost identical. However, we see that, for the qubitlike mode (blue), the piezoelectric coupling to the qubit electric field, which is asymmetric due to the thin lead of the antenna, results in an asymmetric displacement field. This asymmetry is not captured in the unhybridized approach. Such a modification of the acoustic mode shape could lead to additional loss through imperfect mode confinement. Studying these effects using the techniques described in the previous section will be the subject of future work.

[1] Y. Chu and S. Gröblacher, A perspective on hybrid quantum opto- and electromechanical systems, Appl. Phys. Lett. **117**, 150503 (2020).

[2] A. Clerk, K. Lehnert, P. Bertet, J. Petta, and Y. Nakamura, Hybrid quantum systems with circuit quantum electrodynamics, Nat. Phys. **16**, 257 (2020).

[3] G. S. MacCabe, H. Ren, J. Luo, J. D. Cohen, H. Zhou, A. Sipahigil, M. Mirhosseini, and O. Painter, Nano-acoustic resonator with ultralong phonon lifetime, Science **370**, 840 (2020).

[4] V. Gokhale, B. Downey, D. Katzer, N. Nepal, A. Lang, R. Stroud, and D. Meyer, Epitaxial bulk acoustic wave resonators as highly coherent multi-phonon sources for quantum acoustodynamics, Nat. Commun. **11**, 2314 (2020).

[5] Y. Tsaturyan, A. Barg, E. S. Polzik, and A. Schliesser, Ultracoherent nanomechanical resonators via soft clamping and dissipation dilution, Nat. Nanotechnol. **12**, 776 (2017).

[6] C. T. Hann, C.-L. Zou, Y. Zhang, Y. Chu, R. J. Schoelkopf, S. M. Girvin, and L. Jiang, Hardware-Efficient Quantum Random Access Memory with Hybrid Quantum Acoustic Systems, Phys. Rev. Lett. **123**, 250501 (2019).

[7] M. Pechal, P. Arrangoiz-Arriola, and A. H. Safavi-Naeini, Superconducting circuit quantum computing with nanomechanical resonators as storage, Quantum Sci. Technol. **4**, 15006 (2019).

[8] C. Chamberland, K. Noh, P. Arrangoiz-Arriola, E. T. Campbell, C. T. Hann, J. Iverson, H. Putterman, T. C. Bohdanowicz, S. T. Flammia, and A. Keller, *et al.*, Building a Fault-Tolerant Quantum Computer Using Concatenated Cat Codes, PRX Quantum **3**, 010329 (2022).

[9] I. Pikovski, M. R. Vanner, M. Aspelmeyer, M. S. Kim, and Č. Brukner, Probing Planck-scale physics with quantum optics, Nat. Phys. **8**, 393 (2012).

[10] J.-M. Pirkkalainen, S. Cho, J. Li, G. Paraoanu, P. Hakonen, and M. Sillanpää, Hybrid circuit cavity quantum electrodynamics with a micromechanical resonator, Nature **494**, 211 (2013).

[11] J. J. Viennot, X. Ma, and K. W. Lehnert, Phonon-Number-Sensitive Electromechanics, Phys. Rev. Lett. **121**, 183601 (2018).

[12] A. D. O'Connell, M. Hofheinz, M. Ansmann, R. C. Bialczak, M. Lenander, E. Lucero, M. Neeley, D. Sank, H. Wang, M. Weides, J. Wenner, J. M. Martinis, and a. N. Cleland, Quantum ground state and single-phonon control of a mechanical resonator, Nature **464**, 697 (2010).

[13] Y. Chu, P. Kharel, W. H. Renninger, L. D. Burkhart, L. Frunzio, P. T. Rakich, and R. J. Schoelkopf, Quantum acoustics with superconducting qubits, Science **358**, 199 (2017).

[14] M. Kervinen, J. E. Ramírez-Muñoz, A. Välimaa, and M. A. Sillanpää, Landau-Zener-Stückelberg Interference in a Multimode Electromechanical System in the Quantum Regime, Phys. Rev. Lett. **123**, 240401 (2019).

[15] M. V. Gustafsson, T. Aref, a. F. Kockum, M. K. Ekstrom, G. Johansson, and P. Delsing, Propagating phonons coupled to an artificial atom, Science **346**, 207 (2014).

[16] B. A. Moores, L. R. Sletten, J. J. Viennot, and K. W. Lehnert, Cavity Quantum Acoustic Device in the Multimode Strong Coupling Regime, Phys. Rev. Lett. **120**, 227701 (2018).

[17] K. J. Satzinger, Y. P. Zhong, H.-S. Chang, G. A. Peairs, A. Bienfait, M.-H. Chou, A. Y. Cleland, C. R. Conner, É. Dumur, J. Grebel, I. Gutierrez, B. H. November, R. G. Povey, S. J. Whiteley, D. D. Awschalom, D. I. Schuster, and A. N. Cleland, Quantum control of surface acoustic-wave phonons, Nature **563**, 661 (2018).

[18] P. Arrangoiz-Arriola, E. A. Wollack, M. Pechal, J. D. Witmer, J. T. Hill, and A. H. Safavi-Naeini, Coupling a Superconducting Quantum Circuit to a Phononic Crystal Defect Cavity, Phys. Rev. X **8**, 031007 (2018).

[19] S. E. Nigg, H. Paik, B. Vlastakis, G. Kirchmair, S. Shankar, L. Frunzio, M. H. Devoret, R. J. Schoelkopf, and S. M. Girvin, Black-Box Superconducting Circuit Quantization, Phys. Rev. Lett. **108**, 240502 (2012).

[20] F. Solgun, D. W. Abraham, and D. P. DiVincenzo, Black-box quantization of superconducting circuits using exact impedance synthesis, Phys. Rev. B **90**, 134504 (2014).

[21] F. Solgun, Ph.D. thesis, RWTH Aachen University (2015). http://publications.rwth-aachen.de/record/465229/files/465229.pdf.

[22] F. Solgun and D. P. DiVincenzo, Multiport impedance quantization, Ann. Phys. (N. Y.) **361**, 605 (2015).

[23] Z. K. Minev, Z. Leghtas, S. O. Mundhada, L. Christakis, I. M. Pop, and M. H. Devoret, Energy-participation quantization of Josephson circuits, npj Quantum Inf. **7**, 1 (2021).

[24] Z. K. Minev, T. G. McConkey, M. Takita, A. D. Corcoles, and J. M. Gambetta, Circuit quantum electrodynamics (cQED) with modular quasi-lumped models. ArXiv:2103.10344 (2021).

[25] COMSOL AB, Stockholm, Sweden, COMSOL multiphysics structural mechanics module user's guide (2017). https://doc.comsol.com/5.3/doc/com.comsol.help.sme/StructuralMechanicsModuleUsersGuide.pdf.

[26] Ansys, Inc., Ansys® high frequency electromagnetic simulation software R2 v. 21.2 (2021). https://www.ansys.com/products/electronics/ansys-hfss.

[27] Cadence Design Systems, AWR microwave office software v. 16 (2022). www.cadence.com/en˙US/home/tools/system-analysis/rf-microwave-design/awr-microwave-office.html.

[28] Sonnet Software, Sonnet Suites® v. 18 (2022). https://www.sonnetsoftware.com/.

[29] COMSOL AB, Stockholm, Sweden, COMSOL Multiphysics® v. 5.6 (2022). www.comsol.com.

[30] P. Arrangoiz-Arriola and A. H. Safavi-Naeini, Engineering interactions between superconducting qubits and phononic nanostructures, Phys. Rev. A **94**, 063864 (2016).

[31] M. F. Gely and G. A. Steele, QuCAT: quantum circuit analyzer tool in Python, New J. Phys. **22**, 013025 (2020).

[32] M. H. Devoret, in *Fluctuations Quantiques/Quantum Fluctuations*, edited by S. Reynaud, E. Giacobino, and J. Zinn-Justin (Elsevier, Amsterdam, 1997).

[33] Y. Chu, P. Kharel, T. Yoon, L. Frunzio, P. T. Rakich, and R. J. Schoelkopf, Creation and control of multi-phonon Fock states in a bulk acoustic-wave resonator, Nature **563**, 666 (2018).

[34] U. von Lüpke, Y. Yang, M. Bild, L. Michaud, M. Fadel, and Y. Chu, Parity measurement in the strong dispersive regime of circuit quantum acoustodynamics, Nat. Phys. **18,** 794 (2022).

[35] H. Paik, D. I. Schuster, L. S. Bishop, G. Kirchmair, G. Catelani, A. P. Sears, B. R. Johnson, M. J. Reagor, L. Frunzio, L. I. Glazman, S. M. Girvin, M. H. Devoret, and R. J. Schoelkopf, Observation of High Coherence in Josephson Junction Qubits Measured in a Three-Dimensional Circuit QED Architecture, Phys. Rev. Lett. **107**, 240501 (2011).

[36] A piezoelectric multiphysics interface exists, but can only couple solid mechanics to the electrostatics interface, which is not suitable for simulating cQED devices. The electrostatics interface is unable to simulate a microwave cavity as it lacks a feature for phase propagation, and does not have a lumped element boundary condition.

[37] J. Yang, *An Introduction to the Theory of Piezoelectricity* (Springer, Springer, New York, 2005), Vol. 9.

[38] COMSOL AB, Stockholm, Sweden, COMSOL multiphysics reference manual (2020). https://doc.comsol.com/5.5/doc/com.comsol.help.comsol/COMSOL˙Reference-Manual.pdf.

[39] D. Corr and J. Davies, Computer analysis of the fundamental and higher order modes in single and coupled microstrip, IEEE Trans. Microw. Theory. Tech. **20**, 669 (1972).

[40] B. Rahman and J. Davies, Penalty function improvement of waveguide solution by finite elements, IEEE Trans. Microw. Theory. Tech. **32**, 922 (1984).

[41] J. R. Winkler and J. B. Davies, Elimination of spurious modes in finite element analysis, J. Comput. Phys. **56**, 1 (1984).

[42] C. Chen, Z. Shang, J. Gong, F. Zhang, H. Zhou, B. Tang, Y. Xu, C. Zhang, Y. Yang, and X. Mu, Electric field stiffening effect in c-oriented aluminum nitride piezoelectric thin films, ACS Appl. Mater. Interfaces **10**, 1819 (2018).

[43] A. Blais, A. L. Grimsmo, S. M. Girvin, and A. Wallraff, Circuit quantum electrodynamics, Rev. Mod. Phys. **93**, 025005 (2021).

[44] J. Koch, T. M. Yu, J. Gambetta, a. a. Houck, D. I. Schuster, J. Majer, A. Blais, M. H. Devoret, S. M. Girvin, and R. J. Schoelkopf, Charge-insensitive qubit design derived from the Cooper pair box, Phys. Rev. A **76**, 042319 (2007).

[45] D. Lachance-Quirion, Y. Tabuchi, A. Gloppe, K. Usami, and Y. Nakamura, Hybrid quantum systems based on magnonics, Appl. Phys. Express **12**, 070101 (2019).

[46] H. Chen, N. F. Opondo, B. Jiang, E. R. MacQuarrie, R. S. Daveau, S. A. Bhave, and G. D. Fuchs, Engineering electron–phonon coupling of quantum defects to a semiconfocal acoustic resonator, Nano Lett. **19**, 7021 (2019).

[47] D. Wigger, K. Gawarecki, and P. Machnikowski, Remote phonon control of quantum dots and other artificial atoms, Adv. Quantum Technol. **4**, 2000128 (2021).

[48] https://zenodo.org/record/8205753.

[49] D. Steck, *Lecture Notes in Quantum and Atom Optics* (2007), revision 0.13.14. https://atomoptics.uoregon.edu/dsteck/teaching/quantum-optics/.

[50] D. Royer, D. Morgan, and E. Dieulesaint, *Elastic Waves in Solids I: Free and Guided Propagation*, Advanced Texts in Physics (Springer Berlin Heidelberg, 1999).

[51] P. Arrangoiz-Arriola, E. A. Wollack, Z. Wang, M. Pechal, W. Jiang, T. P. McKenna, J. D. Witmer, R. Van Laer,

and A. H. Safavi-Naeini, Resolving the energy levels of a nanomechanical oscillator, Nature **571**, 537 (2019).

[52] L. R. Sletten, B. A. Moores, J. J. Viennot, and K. W. Lehnert, Cavity Quantum Acoustic Device in the Multimode Strong Coupling Regime, Phys. Rev. X **9**, 021056 (2019).

[53] COMSOL AB, Stockholm, Sweden, Manually setting the scaling of variables (2023). https://www.comsol.com/support/learning-center/article/Manually-Setting-the-Scaling-of-Variables-52781.

[54] The equipartition theorem only applies to quadratic terms of the Hamiltonian.

[55] C. Wang, C. Axline, Y. Y. Gao, T. Brecht, Y. Chu, L. Frunzio, M. H. Devoret, and R. J. Schoelkopf, Surface participation and dielectric loss in superconducting qubits, Appl. Phys. Lett. **107**, eid 162601 (2015).

[56] K. L. Geerlings, Ph.D. thesis, Yale University (2013). https://qulab.eng.yale.edu/files/2020/10/Kurtis˙Improving-CoherenceSuperconductingQubits.pdf.

[57] S. Galliou, M. Goryachev, R. Bourquin, P. Abbé, J.-P. Aubry, and M. Tobar, Extremely low loss phonon-trapping cryogenic acoustic cavities for future physical experiments, Sci. Rep. **3**, 2132 (2013).